International Journal of Heat and Fluid Flow 29 (2008) 687–702

Contents lists available at ScienceDirect

International Journal of Heat and Fluid Flow

journal homepage: www.elsevier.com/locate/ijhff

Modelling of three-dimensional jet array impingement and heat transfer on a concave surface

T.J. Craft *, H. Iacovides, N.A. Mostafa

Turbulence Mechanics Group, School of Mechanical Aerospace and Civil Engineering, The University of Manchester, Manchester, UK

ARTICLE INFO

Article history:
Received 4 November 2007
Received in revised form 5 March 2008
Accepted 8 March 2008
Available online 25 April 2008

Keywords:
Jet impingement
Heat transfer
Blade cooling
Non-linear EVM
Wall-functions

ABSTRACT

The paper reports computations of the flow and heat-transfer from a row of round jets impinging onto a concave semi-circular surface, designed to reproduce important flow features found in internal turbine blade cooling applications. Linear and non-linear eddy-viscosity models are applied, with wall-functions to cover the near-wall layer. These are shown to capture the overall flow characteristics, including the wall jets created by impingement on the curved surface and the downwashes caused by the collision of these wall jets. Whilst the non-linear model performs slightly better than the linear, both underpredict the turbulence levels close to impingement and in the downwashes.

The standard, log-law based, form of wall-function is found to be inadequate in predicting the heat-transfer, and a more advanced form developed at Manchester (the AWF) is also tested. The exact way in which convective terms are approximated in this latter approach is shown to be crucial, and a form is presented which leads to stable and reasonably accurate solutions that capture the overall pattern and impingement Nusselt number levels shown in measurements, but underpredict heat transfer levels around the jet downwashes.

© 2008 Elsevier Inc. All rights reserved.

1. Introduction

To achieve efficient cooling of blades within a modern gas turbine, internal blade cooling passages are typically employed. The complex geometrical shape of these results in many flow features being present, including separation, reattachment, strong secondary flows and impingement, in addition to system rotation.

There have been many studies, both experimental and computational, of the effects of sharp U-turns and the rib-rougheners that are typically employed in cooling passages to enhance heat-transfer. A recent review is presented in Launder and Iacovides (2007). Other, equally important, features, such as impingement cooling, have received some attention, Mattern and Hennecke, 1996, Akella and Han, 1998, for example, but have not been so widely studied in the context of blade cooling. Whilst there are numerous studies of jet impingement onto flat plates, few have considered impingement onto the type of curved surfaces found within blade cooling passages. Fewer still have studied such flows under the rotating conditions found in blade applications.

Advances in the availability of computing resources mean that it is now feasible to perform numerically accurate simulations of the flow and heat-transfer through internal cooling passages. However, in order to obtain physically accurate results the models of turbulence employed must be capable of correctly representing the diverse and challenging flow features referred to above. The most widely used linear eddy-viscosity schemes are known to fail in many complex flows, including those involving separation and impingement. Full stress transport models have a better physical basis, but are more computationally expensive. As a result, non-linear eddy-viscosity models have received significant interest in recent years, as they have been seen to offer the promise of considerable predictive improvements over linear schemes with only a modest increase in cost. A further consideration in the modelling of these flows is the handling of the near-wall viscosity-affected layer. Whilst the most accurate method is to employ a fine near-wall grid with a turbulence model containing low-Reynolds-number and appropriate near-wall terms, the requirement to resolve this layer fully leads to very high computational costs. Gant, 2002, for example, reported an order of magnitude difference in required cpu time between low-Reynolds-number and wall-function approaches. As a result, wall-function approaches are widely employed for such industrial applications. However, the standard forms adopted are known to give an inaccurate representation of the near-wall flow in most complex flow situations, and so the present work has tested an alternative, more widely applicable, formulation developed by the Manchester (ex UMIST) group.

The present contribution focuses on the prediction of jet impingement onto a concave surface: a situation typically employed for the internal cooling of the leading edge of a blade. Detailed measurements of a relevant flow have been reported by Kounadis (2005) and Iacovides et al. (2005), using an array of jets

* Corresponding author.
E-mail address: tim.craft@manchester.ac.uk (T.J. Craft).

0142-727X/$ - see front matter © 2008 Elsevier Inc. All rights reserved.
doi:10.1016/j.ijheatfluidflow.2008.03.005

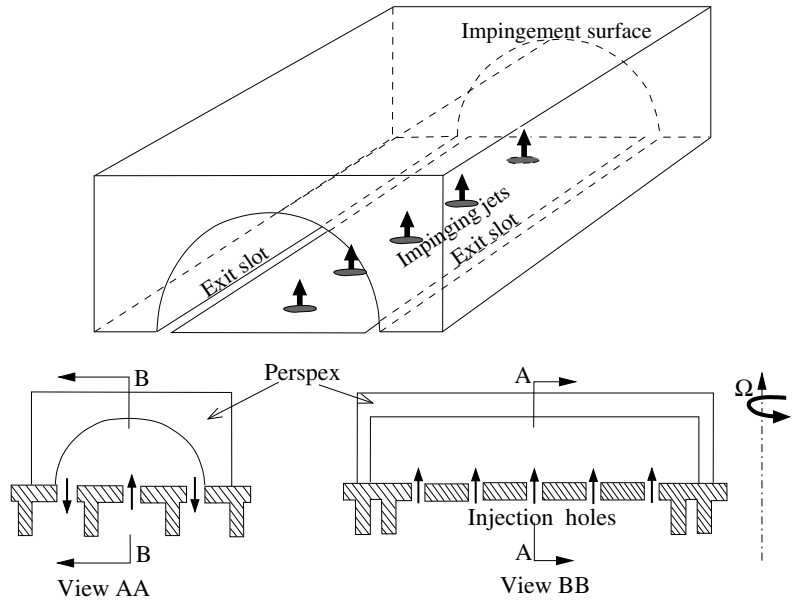

Fig. 1. Geometry of Iacovides et al. (2005).

impinging onto the curved wall of a semi-circular passage, as shown in Fig. 1. This arrangement contains many of the important physical features found in such cooling applications, but is a simple enough geometry, with well-defined boundary conditions, to allow a detailed and informative comparison of computed and measured velocities, stresses and heat-transfer to be made.

The sections below give details of the case studied; the modelling and numerical approaches adopted; present a comparison between the results obtained with different modelling strategies and the measured data, and propose some refinement to the modelling of certain terms within the wall-function approach adopted.

2. Case studied

The case studied experimentally by Iacovides et al. (2005) consisted of a row of five circular jets impinging onto the heated concave surface of a semi-circular passage (see Fig. 1). Heat-transfer measurements were made on the concave surface for a water flow (with molecular Prandtl number of approximately 6), as well as mean velocity and turbulence measurements on a number of planes across the passage. The Reynolds number, based on inlet jet velocity and diameter, was 9400 for the velocity field measurements and 15,000 for the heat-transfer. The whole assembly could

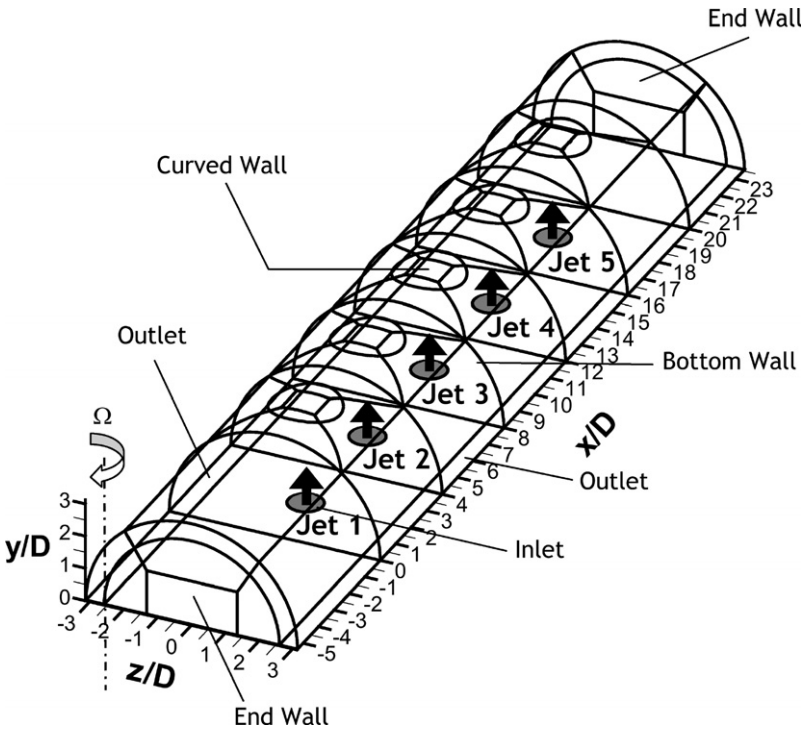

Fig. 2. Five jet computational domain.

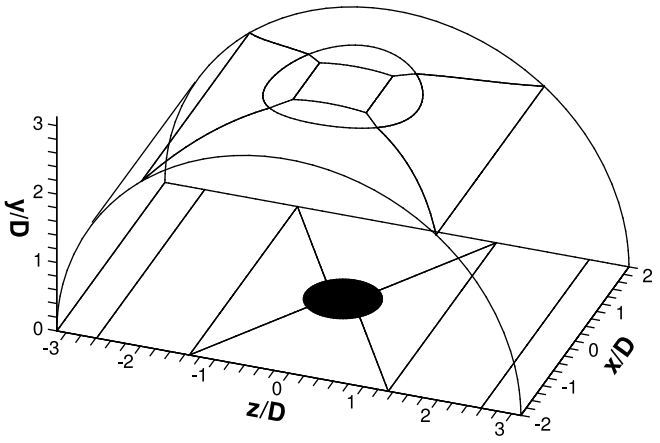

Fig. 3. Single jet computational domain.

be rotated about an axis parallel to that of the jets, in order to study the effect of system rotation. However, simulations reported here are only of non-rotating cases.

The computational domain employed in the present study is shown in Fig. 2. The circular jets enter the domain through the x–z plane, impinge onto the semi-circular outer wall at a height of three jet diameters above the inlets, and the fluid exits the domain via channels half a jet diameter wide, running along the two edges of the base-plane parallel to the x-axis. To match the experimental geometry, the assembly is not quite symmetric in the x direction about jet 3; the distance from the left hand end wall to jet 1 is slightly greater than that between jet 5 and the right hand end wall.

For some modelling explorations, to be described later, computational costs were reduced by simulating only a single jet, on a domain shown in Fig. 3, with symmetry conditions applied on the planes $x/D = \pm 2$. In these latter cases the simulation results are compared to measurements of the central jet shown in Fig. 1.

3. Turbulence modelling

3.1. Fully turbulent flow region

Linear eddy-viscosity models are not expected to capture accurately many of the flow features found in the present complex application. Whilst calculations have, nevertheless, been performed with a linear k–ε model for comparison purposes, the main emphasis in the present study has thus been on the use of non-linear eddy-viscosity models, which have been shown in a number of cases to return results much superior to linear schemes, for only a modest increase in computational cost (see Craft et al. (1996), for example). In this work the model variant detailed by Craft et al. (1999) has been employed, which is a development of the cubic model originally devised by Suga (1995), and has been shown in the above references to perform well in a range of flows, including plane and curved channels and circular jet impingement onto a flat plate.

The linear k–ε model solves transport equations for k and ε of the form

$$\frac{Dk}{Dt} = P_k - \varepsilon + \frac{\partial}{\partial x_k}\left(\frac{\nu_t}{\sigma_k}\frac{\partial k}{\partial x_k}\right), \tag{1}$$

$$\frac{D\varepsilon}{Dt} = c_{\varepsilon 1}\frac{\varepsilon P_k}{k} - c_{\varepsilon 2}\frac{\varepsilon^2}{k} + \frac{\partial}{\partial x_k}\left(\frac{\nu_t}{\sigma_\varepsilon}\frac{\partial \varepsilon}{\partial x_k}\right) \tag{2}$$

and approximates the Reynolds stresses by

$$\overline{u_i u_j} = (2/3)k\delta_{ij} - \nu_t(\partial U_i/\partial x_j + \partial U_j/\partial x_i) \tag{3}$$

Table 1
Model coefficients in the linear and non-linear k-ε models

				Linear	Non-linear					
$c_{\varepsilon 1}$	$c_{\varepsilon 2}$	σ_k	σ_ε	c_μ	c_1	c_2	c_3	c_4	c_6	c_7
1.44	1.92	1.0	1.22	0.09	−0.1	0.1	0.26	$-10c_\mu^2$	$-5c_\mu^2$	$5c_\mu^2$

with $\nu_t = c_\mu k^2/\varepsilon$ and model coefficients given in Table 1.

The non-linear model employed here retains essentially the same transport equations for k and ε, but uses a non-linear relation for the Reynolds stresses:

$$\begin{aligned}\overline{u_i u_j} = {} & (2/3)k\delta_{ij} - \nu_t S_{ij} + c_1\frac{\nu_t k}{\varepsilon}\left(S_{ik}S_{kj} - (1/3)S_{kl}S_{kl}\delta_{ij}\right) \\ & + c_2\frac{\nu_t k}{\varepsilon}\left(\Omega_{ik}S_{kj} + \Omega_{jk}S_{ki}\right) + c_3\frac{\nu_t k}{\varepsilon}\left(\Omega_{ik}\Omega_{jk} - (1/3)\Omega_{lk}\Omega_{lk}\delta_{ij}\right) \\ & + c_4\frac{\nu_t k^2}{\varepsilon^2}(S_{ki}\Omega_{lj} + S_{kj}\Omega_{li})S_{kl} + c_6\frac{\nu_t k^2}{\varepsilon^2}S_{ij}S_{kl}S_{kl} + c_7\frac{\nu_t k^2}{\varepsilon^2}S_{ij}\Omega_{kl}\Omega_{kl},\end{aligned} \tag{4}$$

where the mean strain and vorticity tensors are defined by $S_{ij} = \partial U_i/\partial x_j + \partial U_j/\partial x_i$ and $\Omega_{ij} = \partial U_i/\partial x_j - \partial U_j/\partial x_i$. The turbulent viscosity is again taken as $\nu_t = c_\mu k^2/\varepsilon$, but c_μ is now given by the expression

$$c_\mu = \min\left[0.09, \frac{1.2}{1 + 3.5\eta + f_{RS}}\right] \tag{5}$$

with $f_{RS} = 0.235(\max(0, \eta - 3.333))^2\sqrt{S_I^2}$ and

$$\eta = (k/\varepsilon)\max\left\{\sqrt{S_{ij}S_{ij}/2}, \sqrt{\Omega_{ij}\Omega_{ij}/2}\right\}, \tag{6}$$

$$S_I = S_{ij}S_{jk}S_{ki}/(S_{nl}S_{nl}/2)^{3/2}. \tag{7}$$

Other coefficients are given in Table 1.

As implemented in the computer code, both the above models contain additional low-Reynolds-number and near-wall terms, as detailed in Launder and Sharma (1974) and Craft et al. (1999), respectively. However, with the grid employed in the present calculations, the near-wall viscosity-affected layer is accounted for by the use of wall-functions. The low-Reynolds-number terms in the models thus have a negligible effect and, for clarity, are not described here.

The turbulent heat fluxes are approximated via an eddy-diffusivity approach:

$$\overline{u_i t} = -(\nu_t/\sigma_t)\frac{\partial T}{\partial x_i} \tag{8}$$

with a constant turbulent Prandtl number $\sigma_t = 0.9$.

3.2. Near-wall modelling

One significant problem in 3-D cases such as the present is the handling of the near-wall, viscosity-affected layer. A full resolution of this, with a low-Reynolds-number turbulence model, is very expensive, as a result of the extremely fine grid needed. Hence the present work has used wall-functions to approximate the flow development across this layer, allowing the use of a coarser near-wall grid, with the first near-wall node ideally placed outside the viscous layer, in the fully-turbulent region of the flow.

Standard forms of wall-functions (SWF) are based on an assumed logarithmic mean velocity profile and local equilibrium conditions, leading to the near-wall velocity and temperature profiles being given in non-dimensional form as

$$U^* = (1/\kappa^*)\log(E^* y^*), \quad T^* = \sigma_t[U^* + P^*(\sigma/\sigma_t)], \tag{9}$$

where $U^* = \rho U k_p^{1/2}/\tau_w, T^* = (T_w - T)\rho C_p k_p^{1/2}/\dot{q}_w$, and $y^* = y k_p^{1/2}/\nu$ with τ_w the wall shear stress, $\dot{q}_w$ the wall heat flux, T_w the wall temperature, σ and σ_t the molecular and turbulent Prandtl numbers,

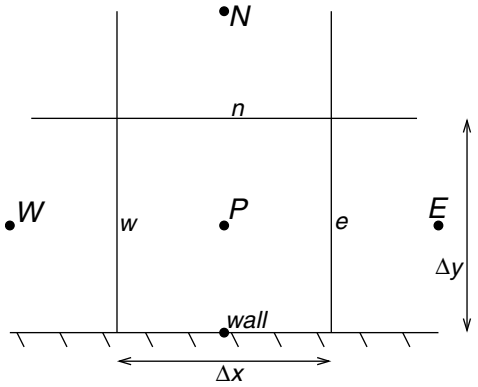

Fig. 4. AWF near-wall grid arrangement.

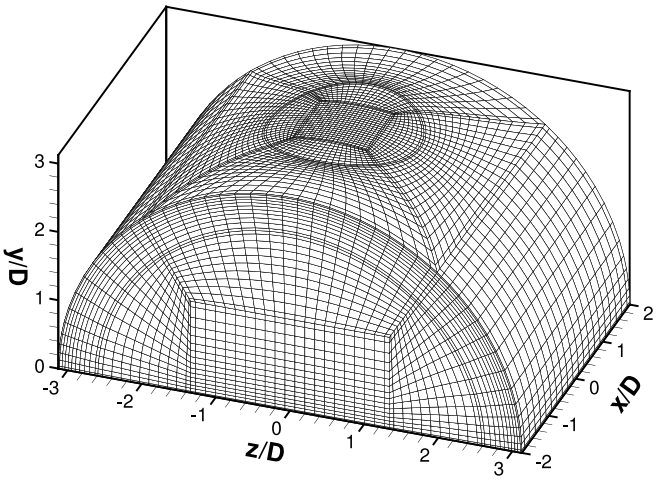

Fig. 5. Details of the single jet computational grid.

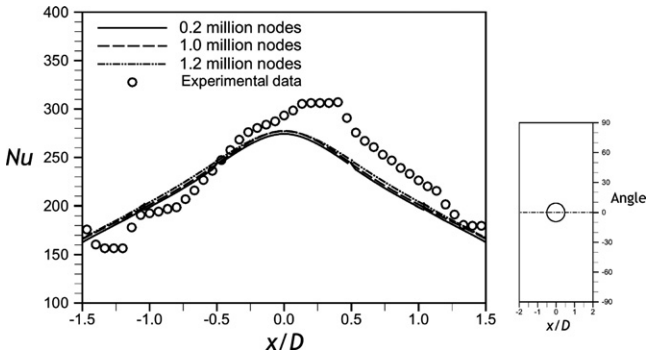

Fig. 6. Nusselt number profiles along the Angle = 0° line for the single jet case using different grids. Lines: computations using the linear EVM and standard wall functions; Symbols: measurements of Iacovides et al. (2005).

y the distance from the wall, k_p the turbulent kinetic energy at the near-wall node, κ^* and E^* constants and P^* the Jayatilleke (1969) pee-function.

However, the above conditions are known to not hold in many situations (including the complex near-wall flow field of the present case). In recent work at Manchester, Craft et al. (2002) developed an improved wall-function approach (the analytic wall-function, or AWF), designed to be more widely applicable. In this approach the assumption is made that the turbulent viscosity increases linearly from the edge of the viscous sublayer, y_v (defined by $y_v^* = 10.8$), to the outer edge of the near wall cell, y_n:

$$\mu_t = \begin{cases} 0 & \text{for } 0 < y < y_v, \\ \mu c_l c_\mu (y^* - y_v^*) & \text{for } y_v < y < y_n \end{cases} \tag{10}$$

with constants $c_l = 2.55$, $c_\mu = 0.09$. One can then write the near-wall mean temperature equation in the simplified form

$$\begin{aligned} &\frac{\partial}{\partial y}\left[\frac{\mu}{\sigma}\frac{\partial T}{\partial y}\right] = \rho U \frac{\partial T}{\partial x} + \rho V \frac{\partial T}{\partial y} \equiv C_{\text{th1}} \quad \text{for } 0 < y < y_v, \\ &\frac{\partial}{\partial y}\left[\mu\left[\frac{1}{\sigma} + \frac{c_l c_\mu}{\sigma_t}(y^* - y_v^*)\right]\frac{\partial T}{\partial y}\right] = \rho U \frac{\partial T}{\partial x} + \rho V \frac{\partial T}{\partial y} \equiv C_{\text{th2}} \\ &\text{for } y_v < y < y_n, \end{aligned} \tag{11}$$

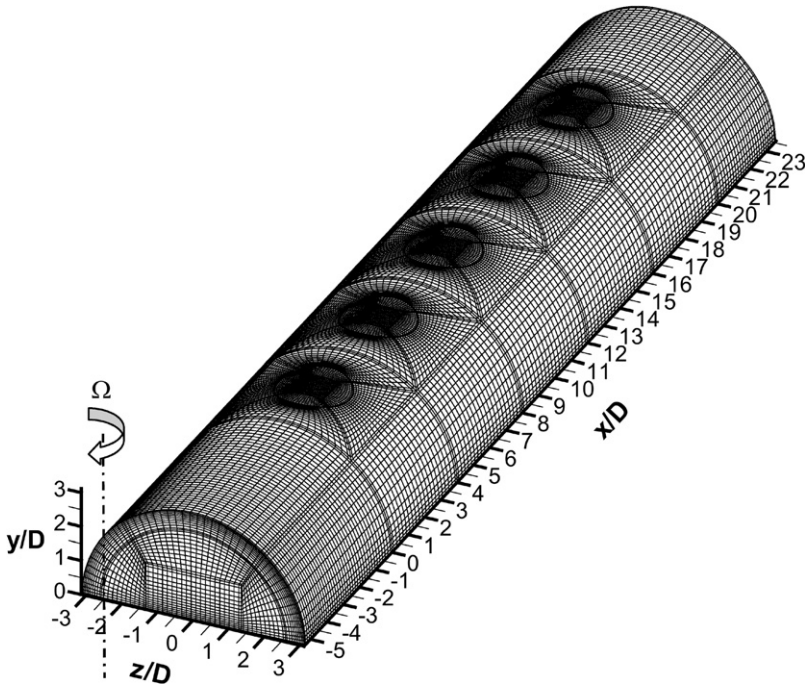

Fig. 7. The five jet array computational grid.

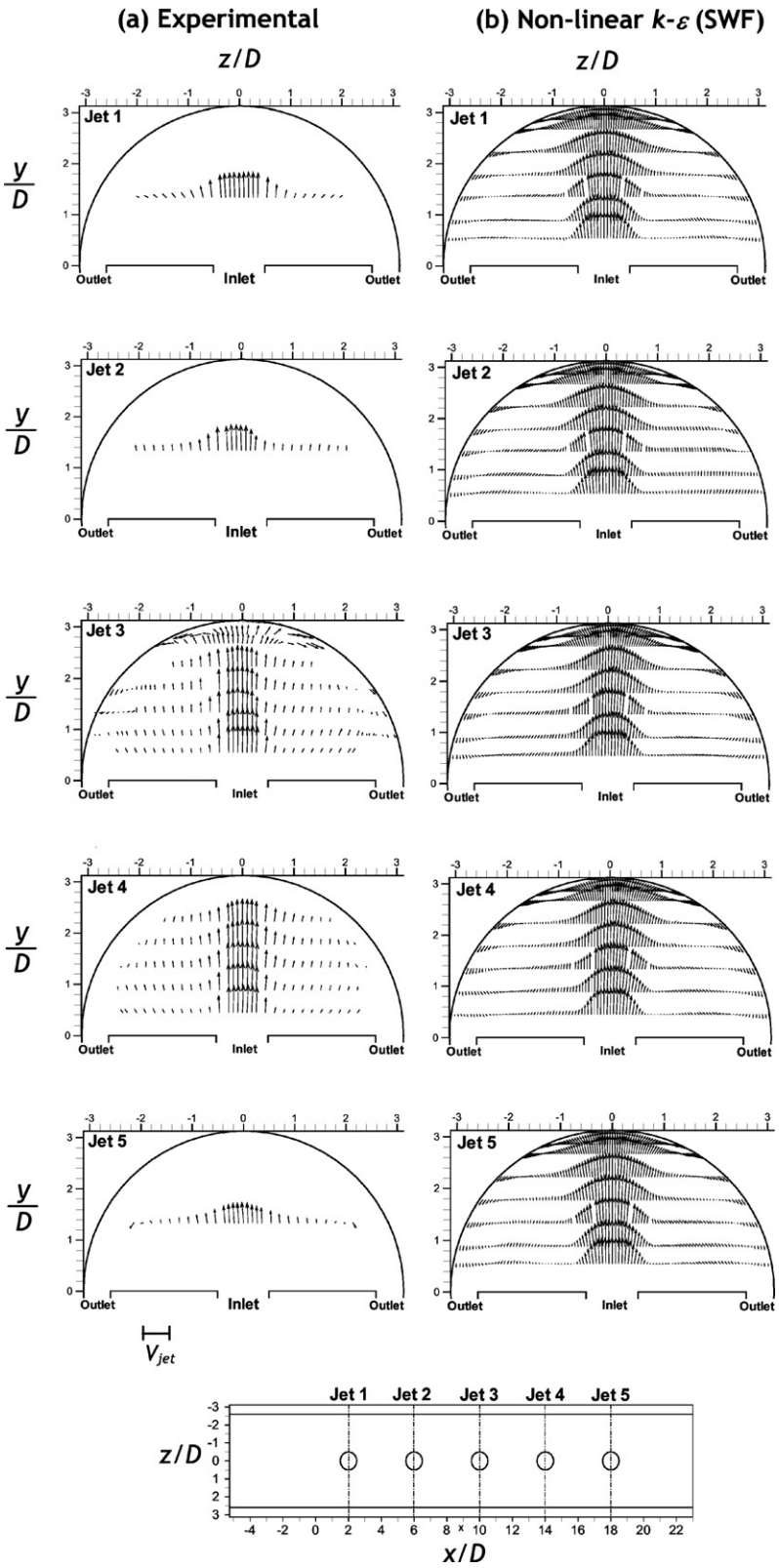

Fig. 8. Predicted and measured velocity vectors on y–z planes through each jet centre: (a) measurements of Iacovides et al. (2005); (b) computations using the non-linear EVM with standard wall function.

where C_{th1} and C_{th2} represent the convective transport terms in the two layers of the cell. If these are assumed constant across each layer, the above equations can be integrated analytically, applying boundary conditions that $T = T_n$ at the outer edge of the cell (see Fig. 4), that T and $\partial T/\partial y$ are continuous at $y = y_v$ and that either the temperature or heat flux are known at the wall.

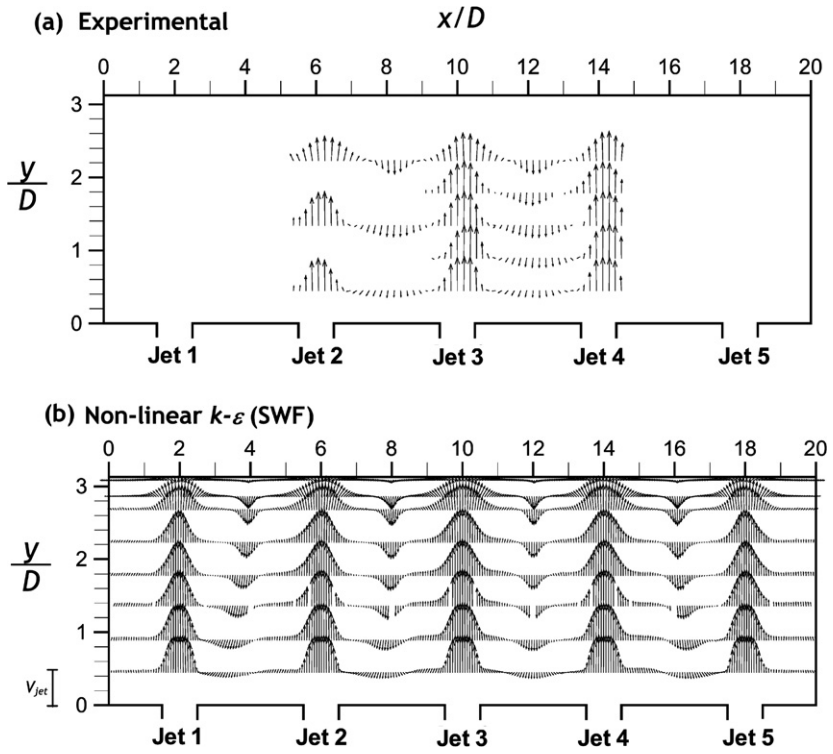

Fig. 9. Predicted and measured velocity vectors on the $z = 0$ plane: (a) measurements of Iacovides et al. (2005); (b) computations using the non-linear EVM with standard wall function.

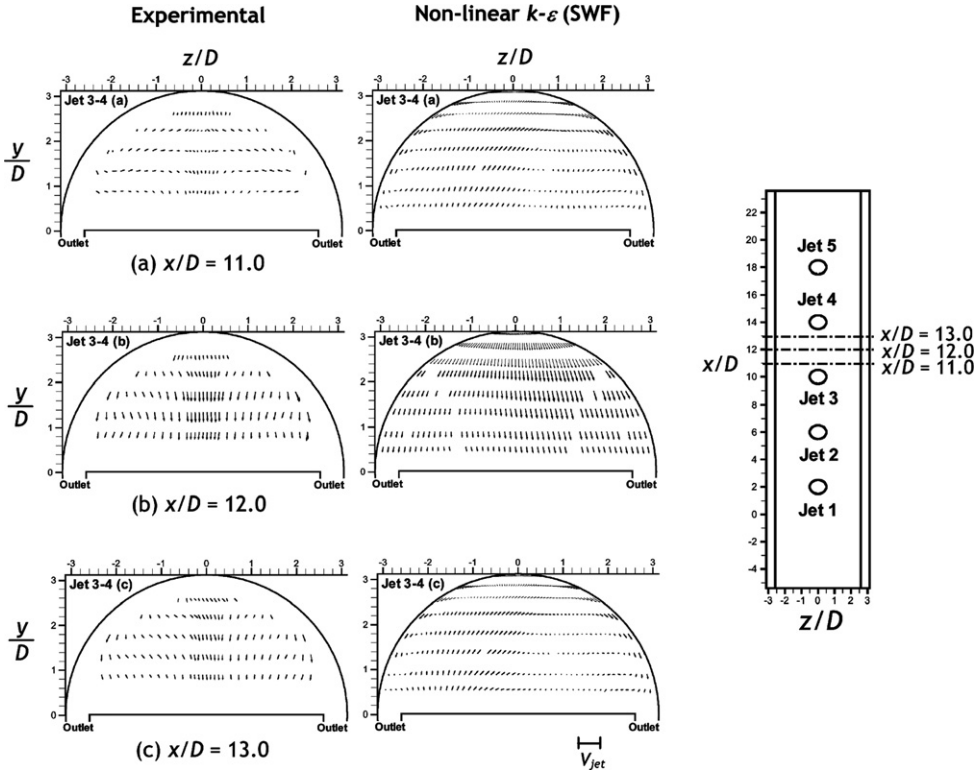

Fig. 10. Predicted and measured velocity vectors on y–z planes between jets 3 and 4: (a) at $x/D = 11$; (b) at $x/D = 12$; (c) at $x/D = 13$. Measurements of Iacovides et al. (2005) and computations using the non-linear EVM with standard wall function.

The result is an analytic expression for the temperature across the near-wall cell, which can be used to set the computational boundary conditions within a wall-function approach. A similar treatment is applied to the wall-parallel momentum equation, where convective and pressure gradient terms now appear in the corresponding expressions to the right-hand sides of Eq. (11):

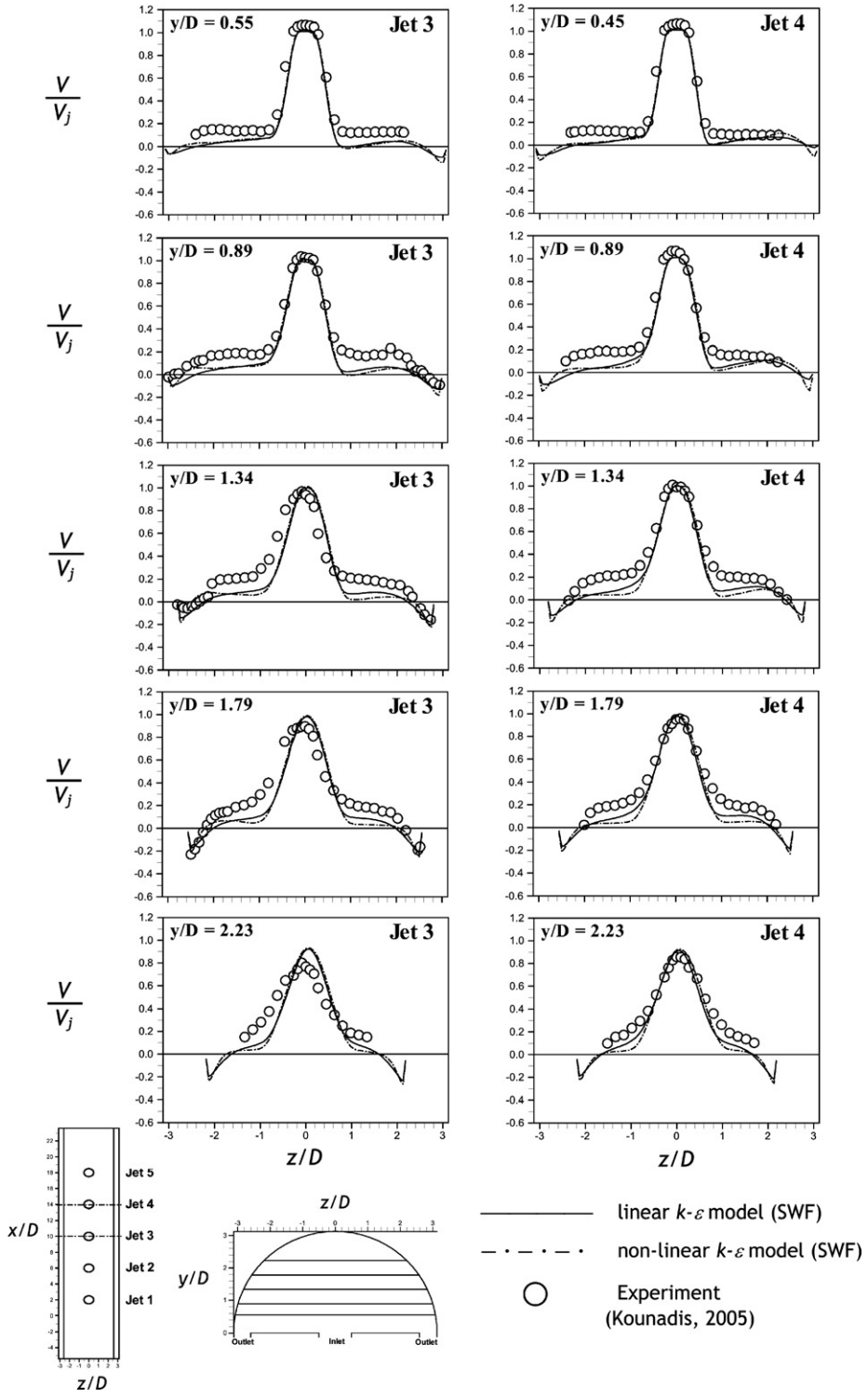

Fig. 11. Vertical velocity profiles in the y–z plane across jets 3 and 4. Lines: present computations; Symbols: measurements of Kounadis, 2005.

$$\frac{\partial}{\partial y}\left[\mu\frac{\partial U}{\partial y}\right] = \rho U\frac{\partial U}{\partial x} + \rho V\frac{\partial U}{\partial y} + \frac{\partial P}{\partial x} \equiv C_{u1} \quad \text{for } 0 < y < y_v,$$
$$\frac{\partial}{\partial y}\left[\mu\left[1 + c_l c_\mu (y^* - y_v^*)\right]\frac{\partial U}{\partial y}\right] = \rho U\frac{\partial U}{\partial x} + \rho V\frac{\partial U}{\partial y} + \frac{\partial P}{\partial x} \equiv C_{u2} \quad \text{for } y_v < y < y_n. \tag{12}$$

An analytic solution of these equations, with boundary conditions that $U = U_n$ at the outer edge of the cell and that U and $\partial U/\partial y$ are continuous at the interface $y = y_v$, allows the wall shear stress to be calculated.

For the turbulent kinetic energy, cell-averaged values of the generation and dissipation rates are evaluated across the near-wall cell. The former is approximated as

$$\overline{P_k} = -\frac{1}{y_n}\int_0^{y_n} \overline{uv}\frac{\partial U}{\partial y}\,\mathrm{d}y = \frac{1}{y_n}\int_{y_v}^{y_n} \nu c_l c_\mu (y^* - y_v^*)\left(\frac{\partial U}{\partial y}\right)^2 \mathrm{d}y, \tag{13}$$

where the velocity gradient $\partial U/\partial y$ is obtained from the analytical solution of Eq. (12). The cell-averaged dissipation rate is obtained by assuming ε to be constant across a thin near-wall layer

($0 < y < y_d$, where y_d^* is taken as 5.1) and that the turbulence lengthscale increases linearly beyond this, resulting in

$$\bar{\varepsilon} = \frac{1}{y_n}\int_0^{y_n} \varepsilon \,\mathrm{d}y = \frac{1}{y_n}\left[\int_0^{y_d} \frac{2\nu k_p}{y_d^2}\,\mathrm{d}y + \int_{y_d}^{y_n} \frac{k_p^{3/2}}{c_l y}\,\mathrm{d}y\right] = \frac{k_p^{3/2}}{y_n}\left[\frac{2}{y_d^*} + \frac{1}{c_l}\log(y_n/y_d)\right]. \quad (14)$$

Finally, the ε boundary condition is applied by setting $\varepsilon_p = k_p^{3/2}/(c_l y_p)$ at the near-wall node. Full details of the derivations and forms employed, and examples of applications, can be found in Craft et al. (2002) and Gerasimov (2003).

A crucial element in applying the AWF to the present problem is the approximation of the convective terms C_{th1} and C_{th2} in the simplified temperature equation (Eq. 11). In the applications referred to above only the convective transport tangential to the wall surface, C_{tht}, was retained, which was simply evaluated in terms of nodal values:

$$C_{\mathrm{th1}} = C_{\mathrm{th2}} = \underbrace{\rho U \frac{\partial T}{\partial x}}_{C_{\mathrm{tht}}} + \underbrace{\rho V \frac{\partial T}{\partial y}}_{C_{\mathrm{thn}}} \approx \rho U_P \left[\frac{T_\mathrm{e} - T_\mathrm{w}}{\Delta x}\right], \quad (15)$$

where quantities at the cell faces e and w were evaluated by interpolating between nodal values at P, E, W as indicated in Fig. 4. However, the applications considered did not include strongly impinging flows such as the present one, and in this case the wall-normal convection, C_{thn}, and the exact form adopted to represent it, become crucially important, as will be apparent in later sections.

4. Numerical treatment

The simulations have been performed using a modified version of the STREAM code (Lien and Leschziner, 1994), which is a finite volume solver employing the SIMPLE pressure correction scheme with Rhie and Chow (1983) interpolation used to avoid chequerboarding arising from the fully collocated grid storage arrangement. The UMIST convection scheme (Leschziner and Lien, 1994) was employed for mean variables, with first order upwind applied for turbulence quantities.

Structured multi-block grids were generated, and Fig. 5 shows details of a typical such grid for the single jet domain. Most of the single jet calculations have been performed on a grid with approximately a quarter of a million cells, with typical near-wall nodes being at a non-dimensional distance of around $y^* \approx 40$ from the wall. Grid refinement tests using a much finer grid of around one million cells were found to give almost identical results to those obtained on the coarser mesh with, for example, the peak Nusselt number predictions differing by less than 2% (see Fig. 6 which shows Nusselt number profiles along $z = 0$, the top of the curved wall). Hence, for computational efficiency, most of the results reported here have been obtained on the coarser mesh.

For the five jet calculations, a grid was built as shown in Fig. 7 by combining five of the single jet grid assemblies, together with additional sections at each end of the domain. This resulted in a grid having approximately 1.3 million cells.

The jet inlet conditions were modelled by applying a constant velocity, turbulence intensity of 15% and viscosity ratio ν_t/ν of 50 across the inlets, except for a band of width $0.2D$ around the outer edge of the jets, where a power-law was fitted to the velocity profile and a mixing-length approximation used to evaluate turbulence levels. This approach helps to form the mixing layer development between the jet and surrounding fluid, and has been tuned in the present case to match available measurements close to the jet inlet. Zero-gradient conditions were applied to all variables at the outlet channels, and all walls were treated with the wall-function approaches described above.

5. Results

5.1. Dynamic field

Fig. 8 shows measured and predicted velocity vectors on y–z planes through the centre of each jet inlet. Computed results are

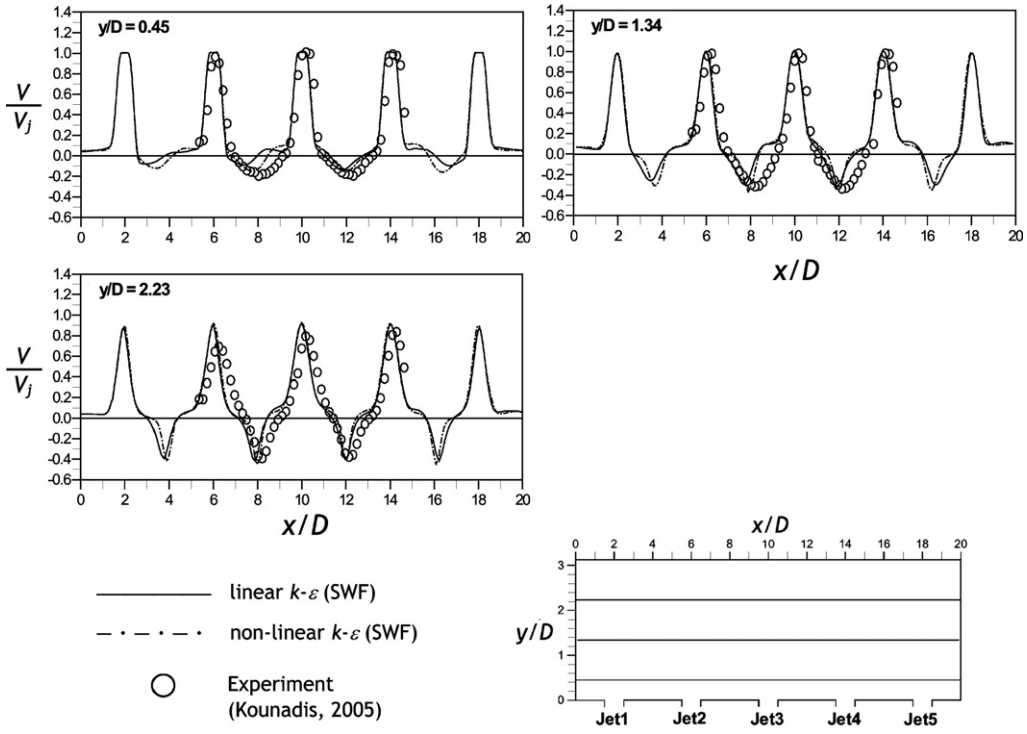

Fig. 12. Vertical velocity profiles in the $z = 0$ plane. Lines: present computations; Symbols: measurements of Kounadis (2005).

shown for the non-linear model with standard wall-functions, although those obtained with other model combinations are almost indistinguishable from these. As shown in the figure, the jets impinge on the curved surface, resulting in a downward directed wall jet developing along this surface. Corresponding vector plots on the symmetry plane $z = 0$ are shown in Fig. 9. As can be seen, the collision of neighbouring impinged wall jets towards the top of the curved surface results in a downward-directed flow midway between the jets. The flow patterns shown in the experimental measurements are broadly reproduced by the simulations, although the predicted downwashes between the jets appear to be somewhat narrower than the measurements, and the upward entrained flow in Fig. 8 appears to be stronger in the measurements than in the simulations. Both measurements and experiments show some asymmetries between the jets (as a result of the geometry not being fully symmetric in the x direction about

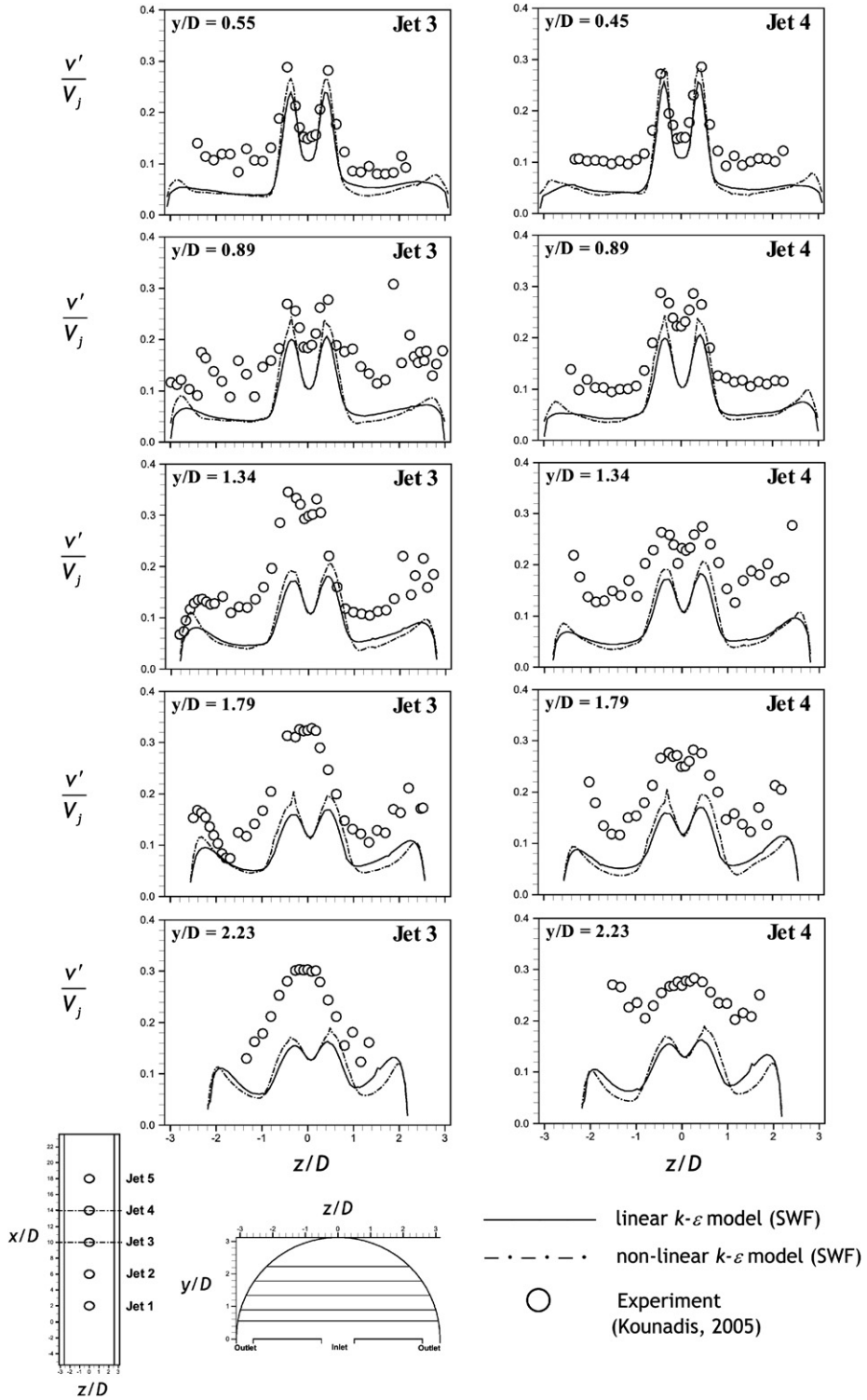

Fig. 13. Rms vertical velocity profiles in the y–z plane across jets 3 and 4. Lines: present computations; Symbols: measurements of Kounadis (2005).

jet 3), although these do not always match each other. For example, the predicted downwash between jets 2 and 3 in Fig. 9 is deflected towards jet 2, whilst that between jets 3 and 4 is more centred between the jets. The measurements, as will become more apparent later, show a slight deflection of these downwashes towards jets 3 and 4, respectively.

Fig. 10 shows vector plots on three y–z planes lying between jets 3 and 4. The central plane clearly shows the downwash flow, that is broadly captured by the simulation. However, the measurements closer to jet 4 (at $x/D = 13$) still show significant downflow, whilst the corresponding ones at $x/D = 11$, close to jet 3, do not, highlighting the slight deflection of the downwash towards jet 4. The simulations show a more symmetric pattern, with a rather similar flow at the two planes $x/D = 11$ and 13.

Fig. 11 shows profiles of the mean vertical velocity at several sections across jets 3 and 4, whilst Fig. 12 shows profiles of the same quantity at a selection of heights on the $z = 0$ plane. Predictions with the linear and non-linear models are included, both using the standard wall-function, since the choice of wall-function was found to have negligible effect on these dynamic field results. As can be seen, both models perform reasonably well, with the non-linear one giving a generally slightly better agreement with the measured data. Both models tend to underpredict the spreading of the main jets towards the top of the domain and, as noted earlier, the downwashes between the jets are predicted as being too narrow, and do not show the same deflections from the mid-jet planes as suggested by the measurements.

Profiles of the rms vertical velocity fluctuations across jets 3 and 4, and in the $z = 0$ plane, are shown in Figs. 13 and 14. Although the levels are reasonably well captured by the simulations close to the jet inlet, at higher positions the turbulence levels in the main jets are underpredicted, consistent with the observation above that the predicted jet spreading appears to be too low. The turbulence levels in the downwash regions are also underpredicted, as shown in Fig. 14, again explaining the rather too narrow downwash flows predicted in the simulations. Corresponding primary turbulent shear stress profiles are shown in Figs. 15 and 16. Again these are in good agreement with the measurements close to the jet inlets, but show a general underprediction of turbulence levels in the upper parts of the main jets and in the vertical downwash regions.

5.2. Thermal field

Whilst the velocity and stress profiles shown above are not particularly sensitive to the wall treatment adopted, the heat-transfer is strongly affected by the choice of wall-function. Initial results will be presented for the single jet geometry described in Section 2, with symmetry conditions imposed at $x/D = \pm 2$. The corresponding dynamic field predictions for this reduced geometry are very similar to a section of those presented above for the full five jet geometry.

Fig. 17 shows the predicted Nusselt number distribution on the curved surface for the linear and non-linear models using the standard wall-function, compared to the measurements across jet 3 of Iacovides et al. (2005). As can be seen, the peak levels predicted in the jet impingement region are rather lower than the measurements. The secondary peaks, shown in the measurements on the centreline at $x/D = \pm 2$ where the jet downwashes occur, are also not captured by the computations. A more quantitative comparison is seen in Fig. 18 which shows profiles of the predicted and measured Nusselt number along the Angle = 0° line (the top of the curved surface). As noted in the contour plots, both model combinations underpredict the peak Nusselt number and return profiles which decrease continuously from the centre to the edges at $x/D = \pm 2$, whilst the measured data show a flatter profile in the outer regions, with small secondary peaks around $x/D = \pm 2$.

Although Fig. 18 suggests the linear EVM gives a better estimate of the peak heat-transfer level than the non-linear scheme, the latter is known to produce a generally more reliable representation of the dynamic field in many complex flows, and it is therefore this

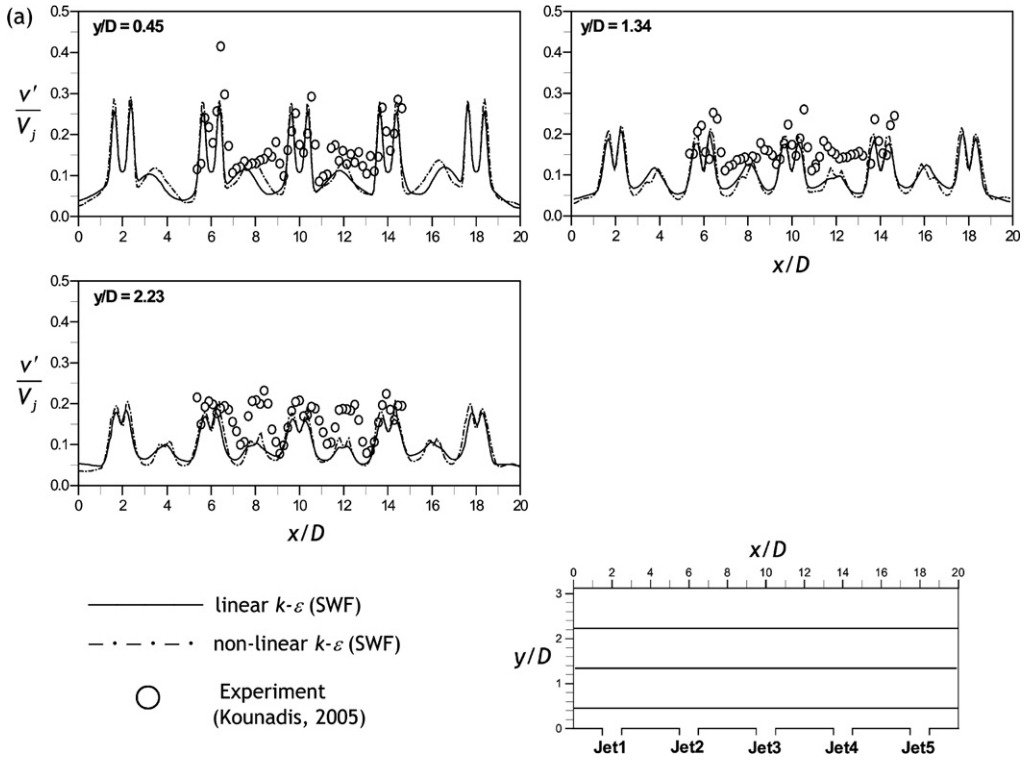

Fig. 14. Rms velocity profiles in the $z = 0$ plane. Lines: present computations; Symbols: measurements of Kounadis (2005).

model that has been tested in combination with the AWF near-wall treatment. As noted in Section 3.2, in the present case, the exact form adopted to model the effects of wall-normal convection of temperature within the AWF has a strong influence on the accuracy of the predictions.

Fig. 19 shows profiles of the Nusselt number along the Angle = 0° line, using the AWF with wall-normal convection ignored (Eq. (15)). Clearly, as might be expected, the result is a significant underprediction of the heat transfer in the impingement region. An initial approach to include wall-normal convection, C_{thn}, within the AWF formulation was to simply treat it in an analogous fashion to the wall-parallel contribution, approximating it in terms of nodal values, so

$$C_{th1} = C_{th2} = \rho U_P \left(\frac{T_e - T_w}{\Delta x} \right) + \rho V_P \left(\frac{T_n - T_{wall}}{\Delta y} \right). \quad (16)$$

This inclusion of the wall-normal convection highlighted a problem in that an unstable numerical feedback was encountered in cells

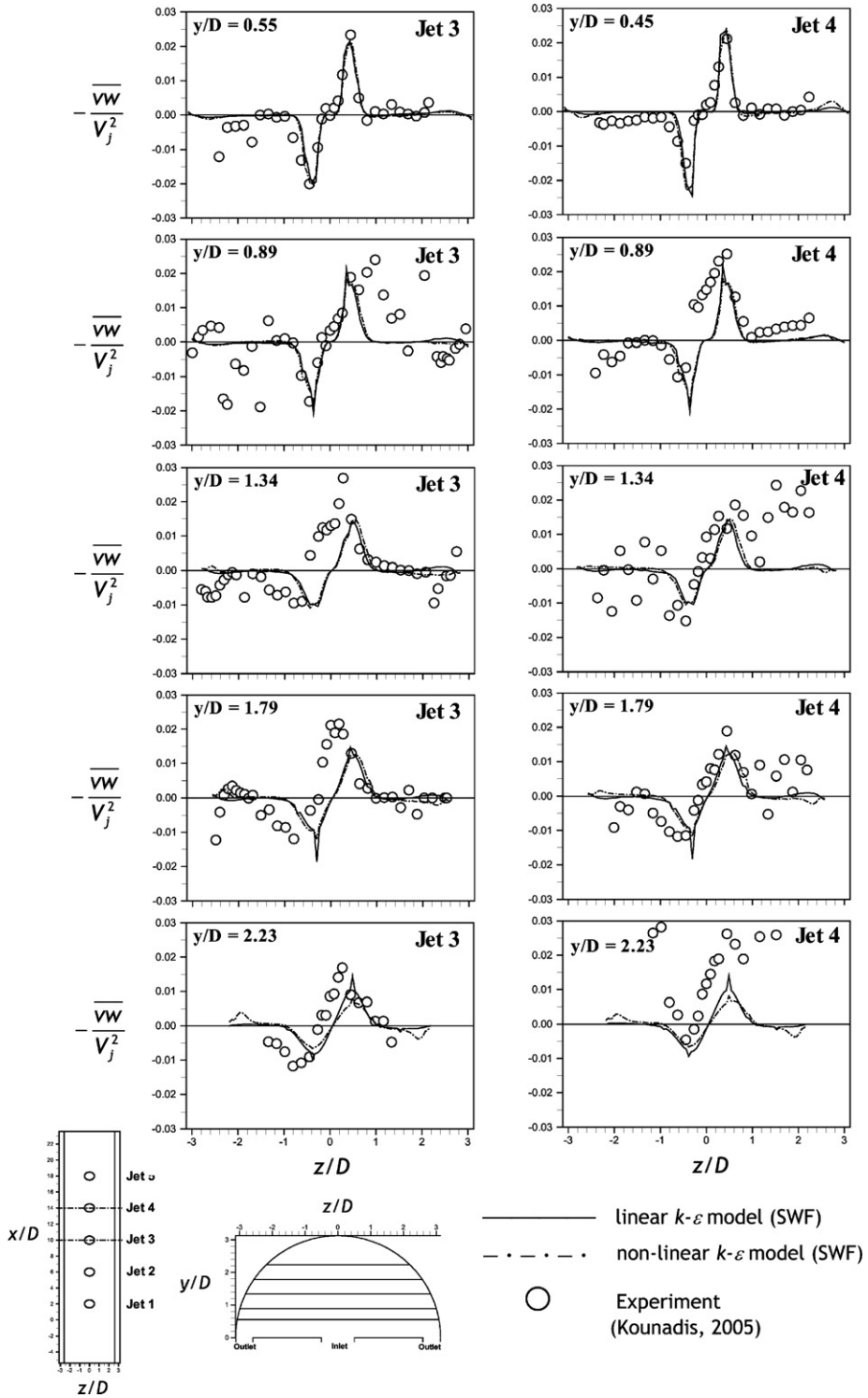

Fig. 15. Turbulent shear stress $\overline{vw}$ profiles in the y–z plane across jets 3 and 4. Lines: present computations; Symbols: measurements of Kounadis (2005).

where the flow was directed away from the wall (around the downwash regions), resulting in very high wall temperatures and numerical instabilities. To prevent this, the wall-normal contribution was only included in the AWF temperature equation when the flow was directed towards the wall. Although this allowed a stable solution to be obtained, use of Eq. (16) proved to be far from accurate, resulting in a peak stagnation point Nusselt number of over 600.

The problem with the approximation of Eq. (16) is, of course, that in reality most of the temperature variation normal to the wall occurs across the thin viscosity-affected layer, where the velocity is relatively small. As a result, the use of the nodal velocity, V_P, and an assumed linear variation of temperature across the cell is highly inaccurate. In an attempt to model the variations of the convective terms across the cell in a more accurate manner, the convection contributions C_{th1} and C_{th2} were approximated by obtaining "average" values for $U\partial T/\partial x$ and $V\partial T/\partial y$ across the two layers $0 < y < y_v$ and $y_v < y < y_n$, respectively

$$C_{th1} = \frac{1}{y_v}\int_0^{y_v} \rho[U(\partial T/\partial x) + V(\partial T/\partial y)]\,dy, \tag{17}$$

$$C_{th2} = \frac{1}{(y_n - y_v)}\int_{y_v}^{y_n} \rho[U(\partial T/\partial x) + V(\partial T/\partial y)]\,dy. \tag{18}$$

The integrals were evaluated numerically using the analytical profiles for U and $\partial T/\partial y$; approximating the wall-parallel gradient as $\partial T/\partial x \approx (T_e - T_w)/\Delta x$, and taking an assumed variation for the wall-normal velocity V across the cell. After testing a number of alternatives, the form adopted for the variation of V was a quadratic increase across the sublayer $0 < y < y_v$, followed by a piecewise linear variation through V_P and V_n, as shown in Fig. 20. An entirely analoguous treatment has also been applied to the convection

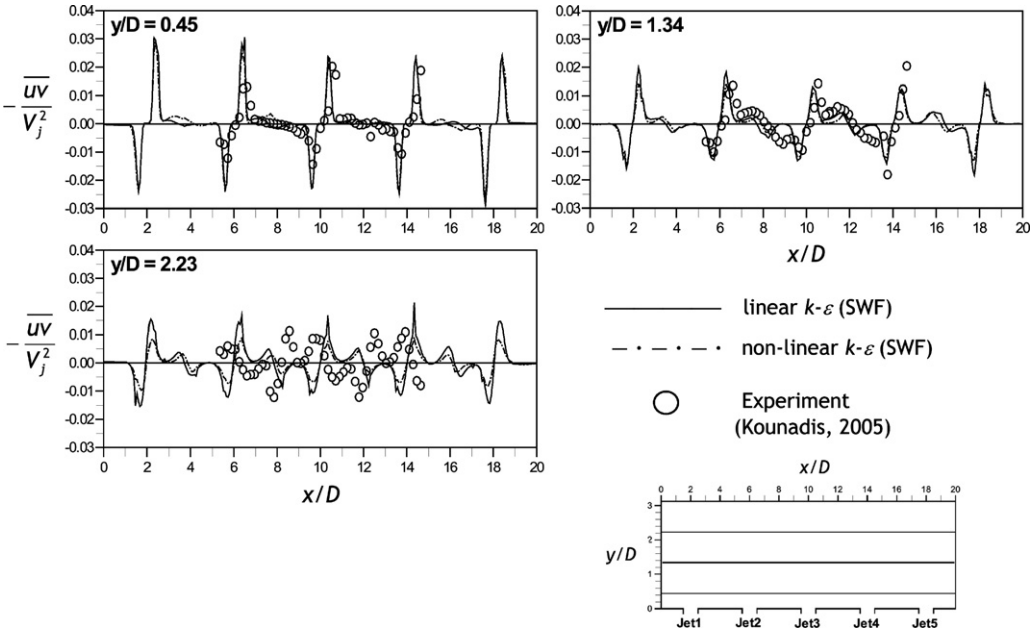

Fig. 16. Turbulent shear stress $\overline{uv}$ profiles in the $z = 0$ plane. Lines: present computations; Symbols: measurements of Kounadis (2005).

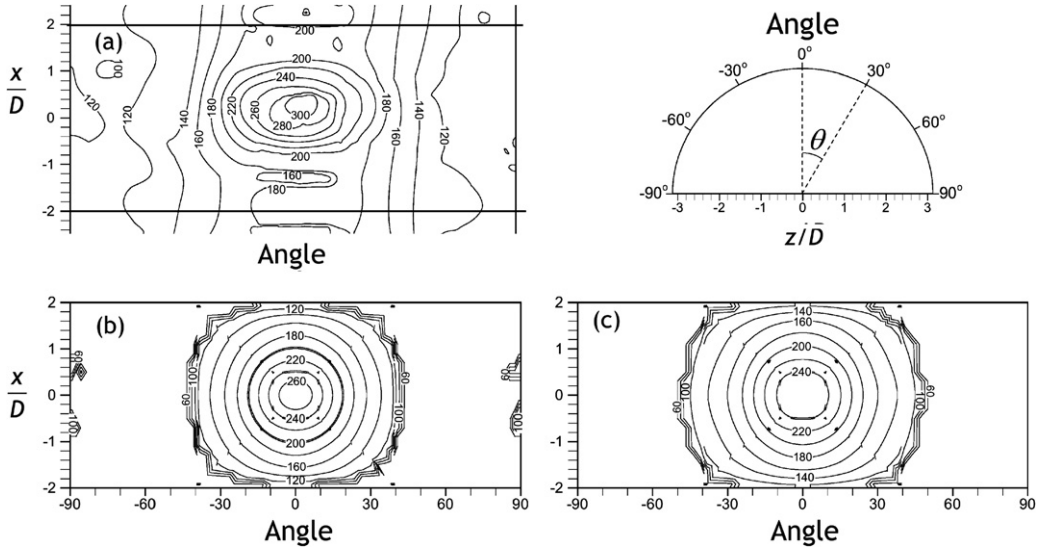

Fig. 17. Nusselt number on the curved surface computed with standard wall-functions: (a) measurements of Iacovides et al. (2005); (b) linear k–ε; (c) non-linear k–ε.

terms in the simplified momentum equation (see Mostafa, 2007 for details), although this refinement had a relatively minor effect on the predicted heat transfer, as can be seen in Fig. 21.

Whilst the modifications introduced above lead to good predictions around the stagnation region, the heat transfer levels in the downwash regions are underpredicted; although secondary peaks are to some extent resolved, the profile in these regions shows a rather "spiky" behaviour. A final refinement in the wall-function implementation was to include the 'laminarization' parameter proposed by Gerasimov (2003), designed to mimic the effects of the thickening or thinning of the viscous sublayer. This is achieved by modifying the near-wall cell-averaged dissipation rate, $\bar{\varepsilon}$, by the correction factor F_ε:

$$\bar{\varepsilon}_{\text{new}} = F_\varepsilon \bar{\varepsilon}_{\text{original}}. \tag{19}$$

The factor F_ε is a function of the ratio of the shear stress at the viscous sublayer's edge to that at the wall:

$$F_\varepsilon = \begin{cases} 1 + 1.5(1 - \exp(-6.9(\lambda - 0.98))) & \\ \quad \times (1 - \exp(-193(\max(\alpha, 0))^2)) & \text{for } \lambda \geqslant 1, \\ 1 - 0.25(1 - \exp(-(1-\lambda)/\lambda)) & \\ \quad \times (1 - \exp(-11.1(\max(\gamma, 0))^2)) & \text{for } \lambda < 1, \end{cases} \tag{20}$$

where

$$\lambda = \frac{\mu_w \sqrt{\left(\frac{\partial U_i}{\partial x_j}\right)^2_w}}{\mu_v \sqrt{\left(\frac{\partial U_i}{\partial x_j}\right)^2_v}}, \tag{21}$$

$\alpha = \lambda/1.02 - 1$ and $\gamma = 0.98/\lambda - 1$. In implementing this function it was necessary to introduce a small amount of local 'smoothing' to the value of λ used in Eq. (20), to avoid numerical problems at a few points where the shear stress at y_v became very small, resulting in a locally very large value for λ. The resulting Nusselt number profile along the Angle = 0° line (Fig. 22) shows a slightly reduced peak value, and the overall level in the downwash regions is still too low.

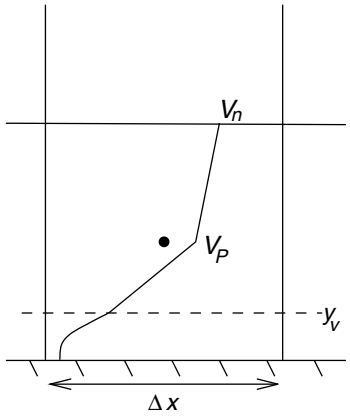

Fig. 20. Assumed wall-normal velocity variation for approximating convection in the AWF.

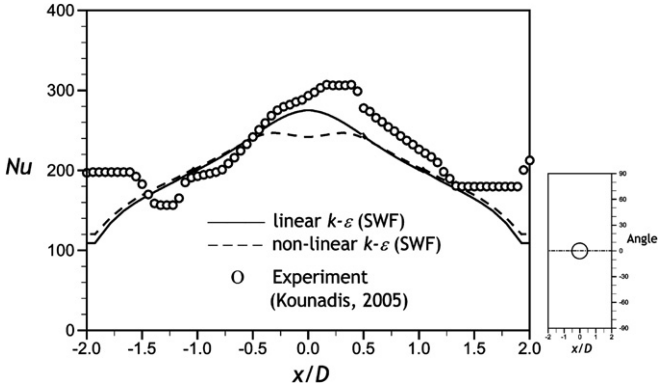

Fig. 18. Nusselt number profiles on the curved surface along the line Angle = 0°. Lines: predictions using standard wall-functions; Symbols: measurements of Kounadis (2005).

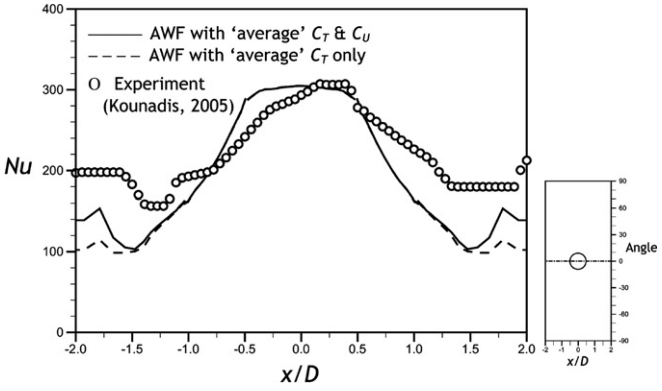

Fig. 21. Nusselt number profiles along the Angle = 0° line. Lines: predictions using the AWF with cell-averaged convection contributions; Symbols: measurements of Kounadis (2005).

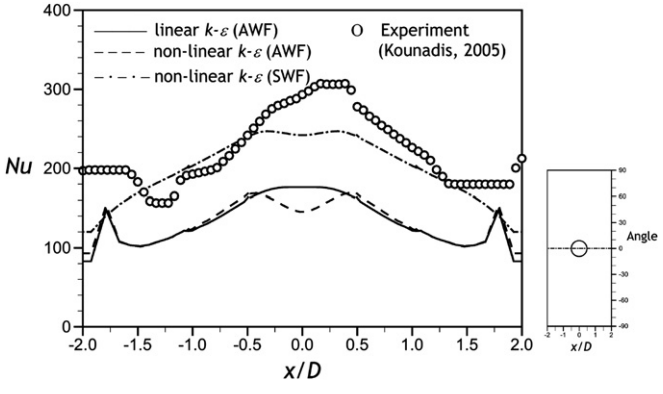

Fig. 19. Nusselt number profiles along the Angle = 0° line. Lines: predictions using the AWF with no wall-normal convection contribution; Symbols: measurements of Kounadis (2005).

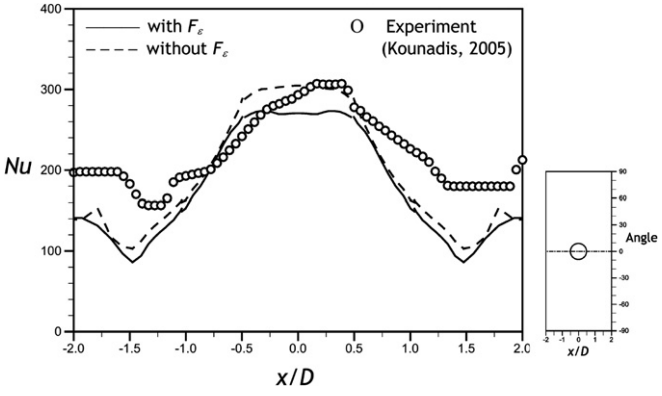

Fig. 22. Nusselt number profiles along the Angle = 0° line. Lines: predictions using the AWF with cell-averaged convection contributions and laminarization parameter; Symbols: measurements of Kounadis (2005).

However, the secondary peaks are now smooth and of the correct qualitative shape.

Fig. 23 shows the resulting Nusselt number contours from applying the standard wall function and the above modified AWF, in conjunction with the linear and non-linear EVM's, to the five jet array geometry. Corresponding profiles along the Angle = 0° line are shown in Fig. 24. As in the single jet geometry, the standard wall function leads to underpredicted peak values of heat transfer, no secondary peaks associated with the downwash regions and, as a result, contour shapes that are rather more circular than the elliptic ones shown by the measurements. The AWF predictions show contour shapes that more closely resemble the measured ones, and peak values close to the measurements. In the downwash regions the heat transfer levels are underpredicted, but clear secondary peaks are visible, with the non-linear model giving overall slightly better predictions than the linear k–ε scheme.

Although the above modelling developments have been presented within the context of the present, rather complex, geometry, it should be noted that they have also been tested in the more generic case of a single circular air jet impinging onto an infinite, flat, heated plate. Fig. 25, for example, shows Nusselt number results for a case at a Reynolds number (based on jet velocity and diameter) of 70,000, impinging from a distance of six jet diameters. The standard wall function is seen to underpredict heat transfer levels around the stagnation region, whilst the original AWF formulation results in a large peak slightly away from the stagnation point. The modifications to the AWF as described above lead to sig-

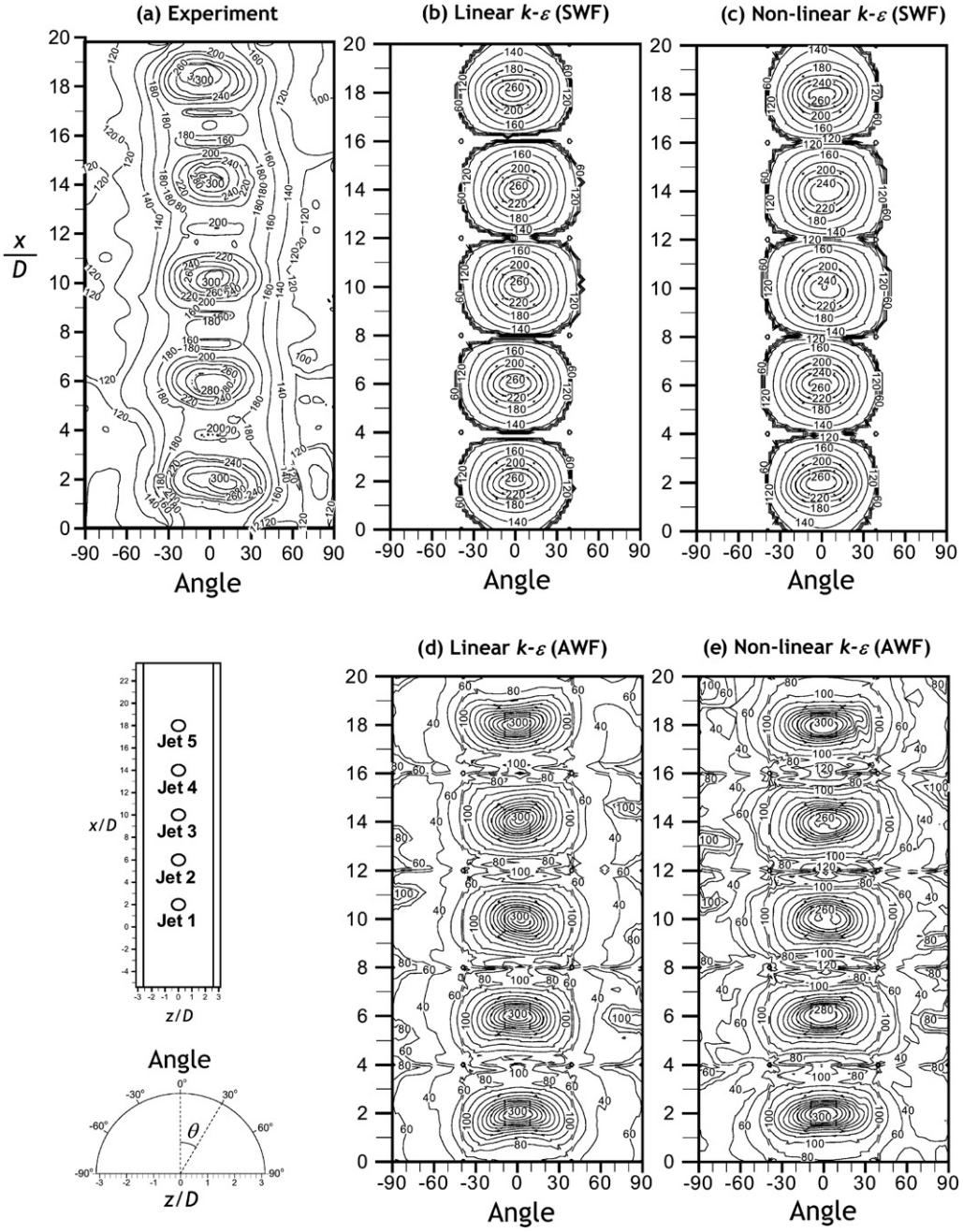

Fig. 23. Nusselt number contours for the five jet array. (a) measurements of Iacovides et al. (2005); (b) linear k–ε with standard wall function; (c) non-linear k–ε with standard wall function; (d) linear k–ε with AWF; (e) non-linear k–ε with AWF.

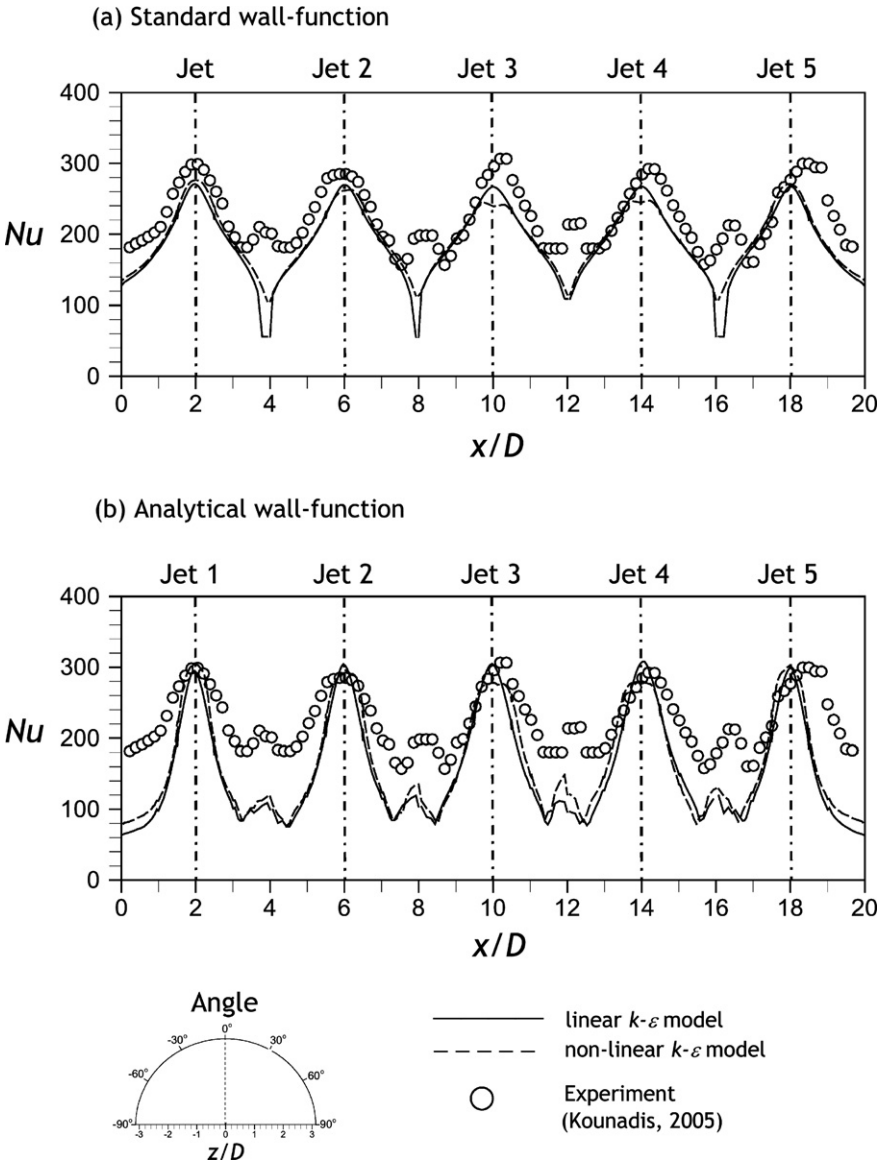

Fig. 24. Nusselt number profiles along the Angle = 0° line for the five jet array. (a) calculations with standard wall function; (b) calculations with AWF. Lines: present calculations; Symbols: measurements of Kounadis (2005).

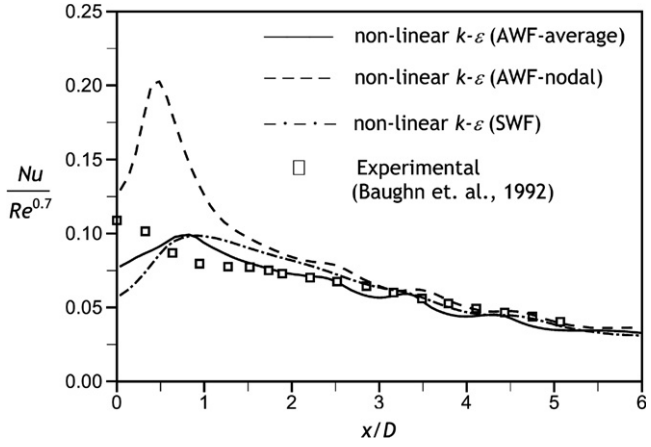

Fig. 25. Nusselt number distributions for a single circular jet impinging onto a flat plate. Calculations using the non-linear k–ε model with the original AWF where convection is based on nodal values (broken line); the present AWF where convection is based on integrated averages (solid line), and standard wall function (chain line). Measurements of Baughn et al. (1992).

nificantly improved results around the impingement zone whilst, as expected, not significantly influencing heat transfer levels at larger radial distances. See Mostafa (2007) for further details.

6. Conclusion

When applied to the present configuration of an array of jets impinging onto a concave surface both the linear and non-linear eddy-viscosity schemes broadly reproduce the mean flow field. Although the non-linear model produces the slightly better turbulence stress levels, both schemes appear to underpredict the levels of turbulence energy as the jets approach the curved surface, and subsequently in the downwash regions.

The use of standard wall-functions results in underpredicted heat-transfer levels around the jet impingement, and a failure to capture the secondary Nusselt number peaks associated with the jet downwashes. The AWF results are highly sensitive to the approximation adopted to represent wall-normal convective transport in this impingement-dominated flow. The proposed form was found to be numerically stable and to give broadly the correct peak

Nusselt number levels, together with secondary peaks associated with the jet downwashes, although the overall heat transfer levels are somewhat underpredicted in these region of the flow.

In future studies differential stress transport models might usefully be tested since these can, in principle, better handle the complex strain fields arising from the jet collisions and interactions, and might help to shed light on the apparent underprediction of turbulence levels in the present predictions. A further refinement, to remove the problem of approximating the jet inlet conditions, would be to include the chamber beneath the present jet inlets within the computational domain, thus allowing the flow and turbulence development within this to affect the individual jets. Finally, another aspect of future studies will be to report on the effects of rotation on the system, comparing the model predictions to the measurements of Iacovides et al. (2005).

Acknowledgement

The research has been supported by Tenaga Nasional Berhad, Malaysia.

References

Akella, K., Han, J.-C., 1998. Impingement cooling in rotating two-pass rectangular channels. J. Thermophys. Heat Transfer 12, 582–588.

Baughn, J.W., Yan, X., Mesbah, M., 1992. The effect of Reynolds number on the heat transfer distribution from a flat plate to an impinging jet. In: ASME Winter Annual Meeting.

Craft, T.J., Launder, B.E., Suga, K., 1996. Development and application of a cubic eddy-viscosity model of turbulence. Int. J. Heat Fluid Flow 17, 108–115.

Craft, T.J., Iacovides, H., Yoon, J.H., 1999. Progress in the use of non-linear two-equation models in the computation of convective heat-transfer in impinging and separated flows. Flow, Turbul. Combust. 63, 59–80.

Craft, T.J., Gerasimov, A.V., Iacovides, H., Launder, B.E., 2002. Progress in the generalization of wall-function treatments. Int. J. Heat Fluid Flow 23, 148–160.

Gant, S.E., 2002. Development and application of a new wall function for complex turbulent flows. Ph.D. Thesis, Department of Mechanical, Aerospace and Manufacturing Engineering, UMIST, Manchester.

Gerasimov, A.V., 2003. Development and application of an analytical wall-function strategy for modelling forced, mixed and natural convection flows. Ph.D. Thesis, Department of Mechanical, Aerospace and Manufacturing Engineering, UMIST, Manchester.

Iacovides, H., Kounadis, D., Launder, B.E., Li, J.-K., Xu, Z.-Y., 2005. Experimental study of the flow and thermal development of a row of cooling jets impinging on a rotating concave surface. ASME J. Turbomach. 127, 222–229.

Jayatilleke, C.L.V., 1969. The influence of Prandtl number and surface roughness on the resistance of the laminar sublayer to momentum and heat transfer. Prog. Heat Mass Transfer 1, 193.

Kounadis, D., 2005. Flow and local thermal measurements in stationary and rotating gas-turbine cooling passages. Ph.D. Thesis, University of Manchester.

Launder, B.E., Iacovides, H., 2007. Internal blade cooling: the Cinderella of C&EFD research in gas turbines. Proceedings of the Institute of Mechanical Engineers, Part A. J. Power Energy 221, 265–290.

Launder, B.E., Sharma, B.I., 1974. Application of the energy-dissipation model of turbulence to the calculation of flow near a spinning disc. Lett. Heat Mass Transfer 1, 131–138.

Leschziner, M.A., Lien, F.S., 1994. Upstream monotonic interpolation for scalar transport with application to complex turbulent flows. Int. J. Numer. Methods Fluids 19, 527–548.

Lien, F.-S., Leschziner, M.A., 1994. A general non-orthogonal finite-volume algorithm for turbulent flow at all speeds incorporating second-moment turbulence-transport closure. Comput. Methods Appl. Mech. Eng. 114, 123–167.

Mattern, C., Hennecke, D., 1996. The influence of rotation on impingement cooling. In: ASME Paper 96-GT-161, Int. Gas Turbine and Aero Congress. Birmingham, UK.

Mostafa, N., 2007. Computational studies of blade cooling related turbulent flows. Ph.D. Thesis, University of Manchester.

Rhie, C.M., Chow, W.L., 1983. Numerical study of the turbulent flow past an airfoil with trailing edge separation. AIAA J. 21, 1525–1532.

Suga, K., 1995. Development and application of a non-linear eddy viscosity model sensitized to stress and strain invariants. Ph.D. Thesis, Faculty of Technology, University of Manchester.